INTERNATIONAL JOURNAL FOR NUMERICAL METHODS IN FLUIDS
Int. J. Numer. Meth. Fluids 2005; **48**:909–927
Published online 14 March 2005 in Wiley InterScience (www.interscience.wiley.com). DOI: 10.1002/fld.951

A second look at the role of the fast Fourier transform as an elliptic solver

E. J. Avital*,†

Department of Engineering, Queen Mary, University of London, Mile End Rd, London E1 4NS, U.K.

SUMMARY

A fast cosine transform (FCT) is coupled with a tridiagonal solver for the purpose of solving the Poisson equation on irregular and non-uniform rectangular staggered grids. This kind of solution is required for the pressure field during the simulation of the incompressible Navier–Stokes equations when using the projection method. A new technique using the FCT–tridiagonal solver is derived for the cases where the boundaries of the flow regime do not coincide with the boundaries of the computational domain and for non-uniform grids. The technique is based on an iterative procedure where a defect equation is solved in every iteration, followed by a relaxation procedure. The method is investigated analytically and numerically to show that the solution converges as a geometric series. The method is further investigated for the effects of the relative size of the rigid body, the grid stretching, size and aspect ratio. The new solver is incorporated with the direct numerical simulation (DNS) and large eddy simulation (LES) techniques to simulate the flows around a backward-facing step and a 3D rectangular obstacle, yielding results that qualitatively compare well with known results. Copyright © 2005 John Wiley & Sons, Ltd.

KEY WORDS: Poisson equation; incompressible flow; rigid bodies; non-uniform grid

1. INTRODUCTION

A major time-consuming task when simulating unsteady incompressible flow is to achieve a velocity field that is divergence-free every time step. The projection method is widely used for this purpose. The time marching is split to two levels, where in the explicit form of the projection method, the first level accounts for the convection and diffusion terms. The second level projects the velocity field to a divergence-free space using the pressure term [1, 2]. The pressure is found by solving a Poisson equation and this is where a significant portion of the

*Correspondence to: E. J. Avital, Department of Engineering, Queen Mary, University of London, Mile End Rd, London E1 4NS, U.K.
†E-mail: e.avital@qmul.ac.uk

Contract/grant sponsor: EPSRC; contract/grant numbers: GR/R64947/01; GR/SR46239/01

Received 17 April 2004
Revised 15 January 2005
Accepted 7 February 2005

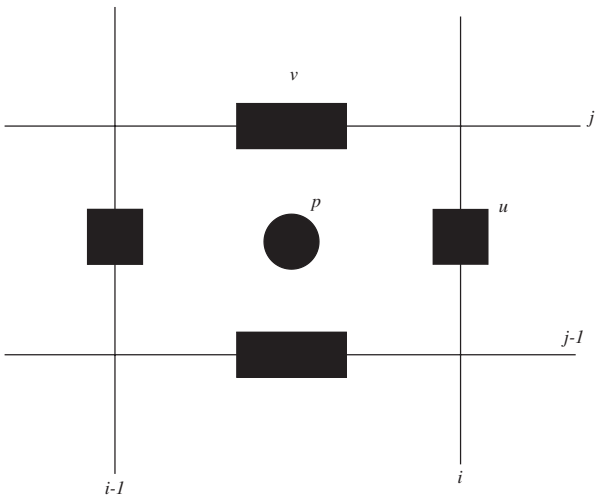

Figure 1. Schematic description of a two-dimensional rectangular staggered grid.

computational time is spent. Other formulations as the stream function–vorticity and velocity–vorticity can also be used to simulate unsteady incompressible flow [1, 3]. However, methods based on those formulations also end up with the need to solve the Poisson equation every time step due to the incompressibility condition. The flow can be made pseudo-compressible as in the artificial compressibility method [1, 4], but a divergence-free velocity field is still required. This is usually achieved by an iterative procedure that can also be time consuming. Here we will deal only with the approach that requires an explicit solution of the Poisson equation and in particular as it is related to the projection method.

One of the earliest rapid elliptic solvers used to solve the Poisson equation was the fast Fourier transform (FFT). By using FFT, one got a set of scalar equations that were easy to solve. A combination of the FFT with a tridiagonal solver was found to be particularly useful for a second-order finite difference scheme based on a uniform rectangular staggered grid (Figure 1). Since the gradient is zero in the boundary condition for the pressure in the projection method [1], fast cosine transforms (FCTs) are used in two directions, while a tridiagonal solver is used in three directions [5]. This results in $O(N_x N_y N_z \log_2(N_x) \log_2(N_z))$ operations, assuming that the tridiagonal solver is used in the y direction and N_x and N_z are powers of 2. A further reduction in the computational time can be achieved by combining it with the cyclic reduction technique, leading to the Fourier and cyclic reduction (FACR) method [6].

The combined FCT and tridiagonal solver approach proved to be effective for cases of simple geometry where a non-uniform grid was needed only in one direction, e.g. boundary layers and cylindrical co-ordinate systems. Furthermore, the technique stayed limited to cases where the flow regime boundaries coincided with the computational box boundaries. This meant that fast iterative solvers as the bi-conjugate gradient (BCG) and multigrid techniques became the preferred elliptic solvers for the general problem [6]. The present work comes to expand the FCT–tridiagonal solver method to cases where the flow regime boundaries do not

coincide with the computational box boundaries and for grids that are non-uniform in more than one direction. The latter can be viewed as an extension of the studies of Cain *et al.* [7], Buell [8] and Avital *et al.* [2] who looked at spectral schemes implemented on rectangular non-uniform collocated grids. Here we will focus our attention on the rectangular staggered grid type that is used along with a second-order central finite difference scheme.

2. MATHEMATICAL AND NUMERICAL FORMULATION

2.1. The projection method and the general FCT–tridiagonal solver approach

The explicit form of the projection method for simulating the incompressible Navier–Stokes (N–S) equations using a rectangular grid can be written as follows [1]:

$$\frac{u_i^* - u_i^n}{\Delta t} = -\frac{\partial(u_i^n u_j^n)}{\partial x_j} + \frac{1}{Re}\frac{\partial^2 u_i^n}{\partial x_j \partial x_j} \tag{1}$$

$$u_i^{n+1} - u_i^* = -\frac{\partial p^{n+1}}{\partial x_i}\Delta t \tag{2}$$

$$\frac{\partial^2 p^{n+1}}{\partial x_i^2} = \frac{1}{\Delta t}\frac{\partial u_i^*}{\partial x_i} \tag{3}$$

where u_i^n and u_i^{n+1} are the velocity components in the n and $n+1$ time stages, respectively. The time accuracy of the scheme is first order but it can be extended easily to a higher order accuracy using, for example, the Runge–Kutta method, see Reference [2] for further details. If the velocity component normal to the boundary is known *a priori*, then the normal component of u^* can be taken as equal to the normal component of u^{n+1} [1]. This is because of the explicit form of the time marching and the use of a staggered spatial grid. Therefore by Equation (2) the gradient of the pressure is zero at the boundary of the computational domain.

The spatial derivatives in (1) should be calculated using schemes of at least of second order. The Poisson equation (3) can be rewritten as $\nabla(\nabla p^{n+1}) = -\nabla u^*/\Delta t$ and is discretized as Equation (2) using a second-order central scheme. This yields the consistent behaviour of the projection method, i.e. an exact divergence-free velocity field if the Poisson equation is solved exactly. Assuming a uniform grid in the x and z directions and using FCTs in these directions, one gets from (3)

$$\frac{s'_j s'_{j-1/2}}{\Delta s^2}\hat{p}_{j+1/2} - \left[\tilde{k}_x^2 + \tilde{k}_z^2 + \frac{(s'_j + s'_{j-1})s'_{j-1/2}}{\Delta s^2}\right]\hat{p}_{j-1/2} + \frac{s'_{j-1}s'_{j-1/2}}{\Delta s^2}\hat{p}_{j-3/2} = \hat{\Gamma}_{j-1/2} \tag{4}$$

where the modified wave number $\tilde{k}_x$ is related to the spectral wave number k_x by

$$\tilde{k}_x^2 = \frac{4\sin^2(k_x \Delta x/2)}{\Delta x^2} \tag{5}$$

$\tilde{k}_z$ is similarly related to k_z. The hat sign denotes a cosine transform in the x and z directions, Γ stands for the source of the Poisson equation, i.e. the right-hand side (RHS) of Equation (3).

s is a uniform co-ordinate that is mapped to the physical non-uniform y co-ordinate through the grid mapping $y(s)$. s' stands for $\mathrm{d}s/\mathrm{d}y$ and j stands for the index in that direction. Equation (4) was discretized in relation to the point $j-1/2$. In the equation for $j=1/2$ $\hat{p}_{-1/2}$ is taken as equal to $\hat{p}_{1/2}$ and at $j=N_y-1/2$ $\hat{p}_{N_y+1/2}$ is taken as equal to $\hat{p}_{N_y-1/2}$ because the gradient of the pressure is zero at the boundary. As long as the compatibility condition is fulfilled, i.e. $\int \bar{u}\cdot \mathrm{d}\bar{A}=0$ over the computational box, there is a pressure solution up to a constant. Equation (4) can be solved using a tridiagonal solver and the pressure in the physical domain can be found using inverse FCTs.

2.2. The case of rigid rectangular bodies

The underlining assumption in (4) is that the grid is single and there are no holes in the grid, meaning the flow fills completely the computational box. However, there are cases where we would like to have holes in the grid, which can be used to model the effect of rigid rectilinear bodies with right angles. The wall velocity boundary conditions can be fulfilled by setting the velocity values on the grid points that are inside the body and are closest to the body's boundary. Such an approach is attractive when the flow regime of interest consists of a much larger space than the rigid bodies and thus the loss in the computer memory allocation due to the 'dead' points inside the rigid bodies is minimal. Examples for such cases are flows around a cube [9], a wall barrier [10] and a rectangular cavity [11].

Numerical experimentation showed that if the RHS of Equation (3) Γ were set to zero inside the rigid body then the solution of Equation (4) would be close to the actual solution of the Poisson equation far from the body but not in the vicinity of the body. Further improvement was achieved when the values of Γ on the grid points inside the body and closest to its boundary were set as equal to the values just outside, i.e. zero gradient of Γ at the boundary. This improvement occurred since the gradient of pressure should be zero at the rigid bodys boundary according to the projection method. However, the solution still was not satisfactory near the rigid body. At this stage two options were considered. The first option was to use this procedure as an approximate solution required for the preconditioned form of the BCG method. This proved to be quite effective when no grid stretching was used in the y direction. However, difficulties rose when grid stretching was used because of the need to solve the transpose matrix equation [6]. Therefore a different approach was developed, which required only the solution of Equation (4) and not its transpose.

The idea is to use the linearity of Equation (4) and instead of solving it for the actual Poisson source, to solve it for a defect source $d=-(L(p_g)-\Gamma)$, where p_g is a guess and L is the Laplace operator, meaning the left-hand side (LHS) of Equation (3). Since the solution of Equation (4) with the actual Poisson source was found to be not that far from the actual solution, then adding the solution of the defect equation to the initial guess should improve it. This leads to an iterative procedure that is stopped when the norm of d is sufficiently small.

Two additional operations were found necessary to accelerate the convergence. Firstly, the highest level of error was found near the rigid body, suggesting a significant contribution coming from the short waves. Relaxation methods as Gauss–Zeidel are excellent in reducing short waves error. Therefore it is strongly recommended to run a few iterations of the point Gauss–Zeidel method to the solution of the defect equation. This is done in the physical space after the defect equation was solved using the FCTs and the tridiagonal solver in the Fourier space and before adding the solution to the pressure of the previous iteration stage.

Secondly, the initial guess for p should be an educated guess that is based on the solution of the previous time step or sub-time step depending on the time marching technique. That solution should be multiplied by the ratio between the two time steps or sub-time steps, see References [2, 12] for examples when a third-order Runge–Kutta method is used for the time marching. Numerical experimentation showed that by doing this the required computational time could be reduced almost by half as the simulation progressed.

To summarize, start from an educated guess for p that is based on a previous solution. Calculate the defect d and implement boundary conditions of zero gradient for d over the rigid body using the body's closest inner grid points. Take d as zero in all the other inner grid points. Solve Equation (4) where $\hat{d}$ is set as the source instead of $\hat{\Gamma}$. Improve the solution by applying a few point Gauss–Zeidel iterations to the defect equation in the physical space. In the following examples, four iterations were found to be sufficient. Add the solution to the initial guess and calculate the defect again. If the norm of the new defect is sufficiently small, for example, as compared to the norm of the actual Poisson source Γ, stop here. Otherwise calculate the next level of solution to the defect equation and continue until convergence.

The proposed method is close in its methodology to the multigrid method by relying on the solution of the defect equation and a relaxation procedure. However, there is only one grid and thus no restriction and prolongation operators are needed. Furthermore, the rigid body boundaries stay well defined and do not change location as often happens when the coarse grids of the geometric multigrid approach are used on grids with holes.

The new iterative method was investigated analytically for the 1D case in Appendix A. It is shown that the pressure solution converges as a geometric series to the analytical solution, where the ratio between the series' terms is the length ratio between the rigid body segment and the total computational domain segment. However, in that analysis the interaction between the modes was not considered. That interaction occurs due to the discontinuity at the boundary of the rigid body. This is the cause of Gibb's phenomenon and its nature is to leak energy to higher modes. Therefore relaxation methods as the point Gauss–Zeidel are quite effective in suppressing this effect as is found in the test cases analyzed in Section 3.

2.3. *Non-uniform grid and FCT*

The transformation of the matrix presentation of the discretized Poisson equation in the physical space to a set of scalar equations in the Fourier space is because of the uniform grid in the directions where the FCTs are used. If the grid is not uniform in that direction then interactions between the FCT modes occur which result in another matrix equation. However, if the grid is only moderately non-uniform then the interaction is weak and using only the dominant diagonal terms in the equation will lead to a solution that is not far from the actual solution. This was the idea behind the work of Avital *et al.* [2] who derived a collocated grid mapping for a spectral scheme and used the BCG method to solve the Poisson equation. Here the iterative procedure based on the defect equation will be considered for the staggered grid instead.

If a grid mapping $x(r)$ is used where r is an equally spaced direction and x is the physical non-equally spaced direction then

$$\frac{\partial}{\partial x}\left(\frac{\partial p}{\partial x}\right)\bigg|_{i-1/2} = \frac{r_i' r_{i-1/2}' p_{i+1/2} - (r_i' + r_{i-1}') r_{i-1/2}' p_{i-1/2} + r_{i-1}' r_{i-1/2}' p_{i+1/2}}{\Delta r^2} + O(\Delta r^2) \qquad (6)$$

The aim is to approximate the RHS of (6) by a similar expression that does not lead to an interaction between the FCTs modes. This will happen if the coefficients of the p's in (6) are constants. Consider for this purpose the mapping of Avital *et al.* [2]

$$\frac{\mathrm{d}r}{\mathrm{d}x} = \alpha + \beta \sin^2(\pi r), \quad 0 \leqslant r \leqslant 1 \tag{7}$$

This mapping was used to concrete grid points in the centre of the computational domain in order to simulate effectively jet flow. It can also be used to concentrate points at the edges of the computational domain as required for example in channel flow, although in that particular case the grid is usually uniform in the other two directions and thus FCTs can be used in those directions.

If all the $\mathrm{d}r/\mathrm{d}x$'s in (6) are evaluated at point $i-1/2$ when using the mapping in (7), one will get

$$\frac{\partial}{\partial x}\left(\frac{\partial p}{\partial x}\right)\bigg|_{i-1/2} = \frac{[\alpha^2 + \alpha\beta + 3\beta^2/8 + f(r_{i-1/2})](p_{i+1/2} - 2p_{i-1/2} + p_{i-3/2})}{\Delta r^2} + O(\Delta r) \tag{8}$$

where the first-order accuracy is due to the evaluation of the r's at point $i-1/2$. $f(r_{i-1/2})$ is a function of the location $r_{i-1/2}$ and the mapping coefficients α and β. If $\beta = 0$, i.e. the grid is uniform, then $f(r_{i-1/2}) = 0$. If $f(r_{i-1/2})$ is neglected in expression (8) then the discretized form of the Poisson equation as expressed in Equation (4) can be recovered but with the modified wave number

$$\tilde{k}_r^2 = (\alpha^2 + \alpha\beta + 3\beta^2/8)\frac{4\sin^2(k_r \Delta r/2)}{\Delta r^2} \tag{9}$$

instead of $\tilde{k}_x^2$. Solving Equation (4) with the modified wave number $\tilde{k}_r^2$ will yield only an approximate solution if $\beta \neq 0$. However, if that solution is not far from the actual solution as in the case of a moderate grid stretching, then the iterative procedure of the defect equation solution described for the rigid body case can be applied here as well. It should be noted that $L(p)$ in the calculation of the defect d is the actual discretized Poisson operator as expressed in Equation (6) for the x direction and not the approximation in Equation (8).

The effect of the stretching factor β/α on the defect was examined for the 1D case by calculating it after one iteration. The differentiation was carried out analytically and the integration required for the L_2 norm calculation was carried out numerically. The results are shown in Figure 2 for various modes of Γ in the r domain, i.e. $\Gamma = \cos(n\pi r)$ where n is the number of the mode. The defect's norm is normalized by $\|\Gamma\|_2$. There is a clear monotonic increase in the normalized norm as β/α increases. This is as expected, however the effect of the ratio β/α decreases with the number of the mode. It means that the long waves are going to be more problematic and these are also the wave lengths where the relaxation procedure is least effective. Therefore in order to achieve a good convergence it can be concluded from Figure 2 that β/α should be kept in the order of 1 and preferably less than 2. This limit is similar to the limit derived by Avital *et al.* [2] for a fast convergence for the BCG method when the spectral scheme was used.

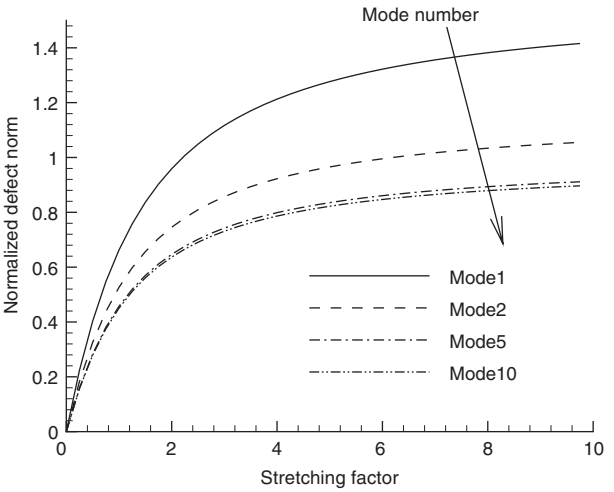

Figure 2. The variation of the L_2 norm of the defect d with the stretching factor β/α of the grid mapping (7) for the 1D case in the continuous limit after one iteration. The defect norm is normalized by the L_2 norm of the Poisson source $\|\Gamma\|_2$, where $\Gamma = \cos(n\pi r)$ and n is the mode number.

3. TEST CASES

The new iterative method was tested on two basic configurations, a two-dimensional rigid body in the form of a backward-facing step and a three-dimensional rigid body in the form of a box.

3.1. The two-dimensional step configuration

A rectangular rigid body is taken as occupying the lower left corner of the computational domain, see Figure 3. This is the configuration of a backward- or forward-facing step, depending on the flow direction. To test the convergence rate of the proposed method an artificial source was prescribed to Equation (3) by taking

$$[u^*, v^*] = [\sin(k_x x)\cos(k_y y), \cos(k_x x)\sin(k_y y)] \tag{10}$$

inside the flow domain and zero inside the rigid body. Δt was taken as 1, $k_x = n\pi/L_x$ and $k_y = n\pi/L_y$, where n is the number of the mode. Flow field (10) fulfils the compatibility condition and thus the Poisson equation should have a unique solution up to a constant. The FCT was applied in the x direction and the tridiagonal solver was applied in the y direction in the following cases.

The effect of the mode number on the number of iterations it takes to reach a normalized defect norm less than 10^{-5} is shown in Figure 4. The geometric configuration is of $L_x = 2L_y$, $a/L_x = h/L_y = 0.5$ and the grid size in $(N_x, N_y) = (129, 65)$. Since a staggered grid is used, only $(N_x - 1, N_y - 1)$ grid points are actually used for the solution of the Poisson equation and those numbers are integer powers of 2. It is evident from Figure 4 that as n increases the number of iterations decreases and it points to the better performance of the method for the

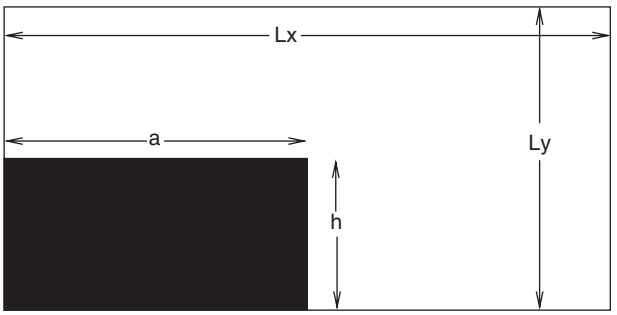

Figure 3. Schematic description of the two-dimensional rigid body configuration to be tested and whose results are shown in Figures 4–8.

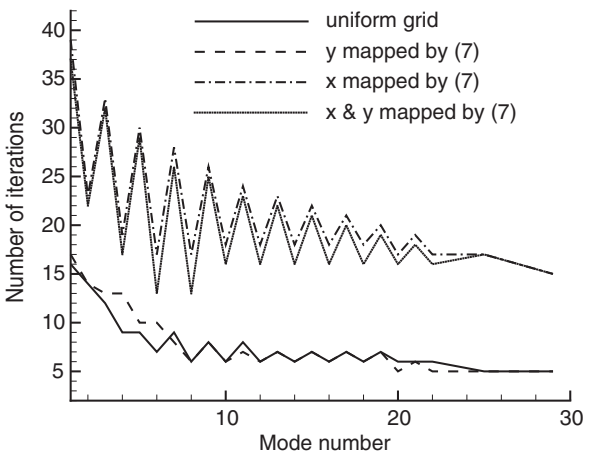

Figure 4. The effect of the mode number on the number of iterations it takes to get a normalized defect norm $\|d\|_2/\|\Gamma\|_2$ lower than 10^{-5} for the rigid body configuration shown in Figure 3. The rigid body size is $a/L_x = h/L_y = 0.5$ where $L_x = 2L_y$ and the grid's number of points is $(N_x, N_y) = (129, 65)$. The mode number and the Poisson source are defined in Equation (10). The FCT is used in the x direction and the tridiagonal solver is used in the y direction. If the grid mapping (7) is used, then the grid stretching factor β/α is 1.

short waves as was already indicated in Figure 2. The uniform grid shows in general the best performance in terms of convergence rate as one might have expected. However, the grid with a non-uniform y direction also shows a similar convergence rate. This is encouraging because the tridiagonal solver by its own is capable of dealing with grid stretching without any deterioration of performance. The result in Figure 4 demonstrates that this capability was not damaged by the introduction of the rigid body, at least in this particular case.

The relatively slow convergence in the grids with a non-uniform x direction as seen in Figure 4, is also as expected. This is because the iterative method has also to deal with the non-uniformity of the grid in the direction where the FCT is used. A bit surprising is the

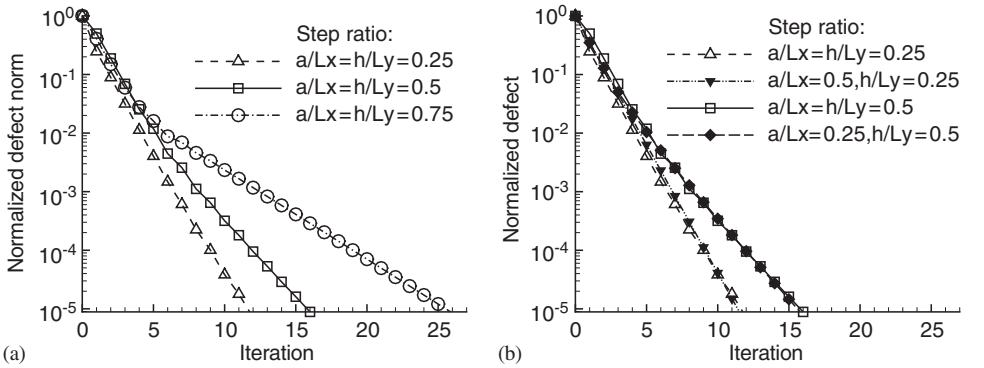

Figure 5. The effect of the rigid body's size and aspect ratio on the convergence rate, when the aspect ratio is: (a) fixed; and (b) varied. The grid is uniform and the Poisson source is of Mode 1. The rigid body is defined in Figure 3 and the rest of the conditions are as in Figure 4.

result that the non-uniform grid in both x and y directions shows a slightly better convergence rate than the grid with the non-uniform x direction only. It should be noted that the slower convergence of the non-uniform grid should not deter its usage. For example such a grid can be useful to capture the extremely thin boundary layer developing on the normal wall of the forward-facing step. Nevertheless, grid stretching in the FCT direction should be used with caution due to its undesirable effect on the convergence rate.

The effects of the relative size of the rigid body and its aspect ratio on the convergence rate are demonstrated in Figure 5 for the uniform grid case and for Mode 1. This is the mode that took the longest to converge by Figure 4. Initially the effects of the rigid body size and aspect ratio are small. However, as the iterative procedure proceeds, the effect of the rigid body size becomes evident in Figure 5(a). All sizes show a convergence rate of a geometric series as predicted by the 1D analysis in Appendix A. Furthermore, the slopes of the lines are close to the inverse of the step ratio. This particularly holds for the step ratios of 0.5 and 0.75. This finding is also in a very good agreement with the analysis given in Appendix A, showing that the interaction between the modes that was neglected in that analysis did not spoil the convergence. However, it should be noted that when the relaxation stage of the Gauss–Zeidel was removed, the convergence rate deteriorated considerably after a few iterations, pointing to the importance of that stage. The effect of the aspect ratio of the rigid body is shown in Figure 5(b). It is seen that the 1D estimate of the convergence rate can be taken as an estimate for the lower limit if the longest length of the body is considered. The convergence rate shows higher sensitivity to the length in the y direction than to the x direction where the FCT is used. However when this 2D effect becomes significant it only improves and does not spoil the convergence rates seen in Figure 5(a).

The effect of the grid mapping on the convergence rate is further demonstrated in Figure 6. As expected from the results in Figure 4, the convergence rate deteriorates considerably when the grid is stretched in the x direction, which is where the FCT is used. Nevertheless the convergence rate still exhibits the behaviour of a geometric series, pointing to the dominance of this convergence mechanism even when a grid mapping is added. The effect of the grid size

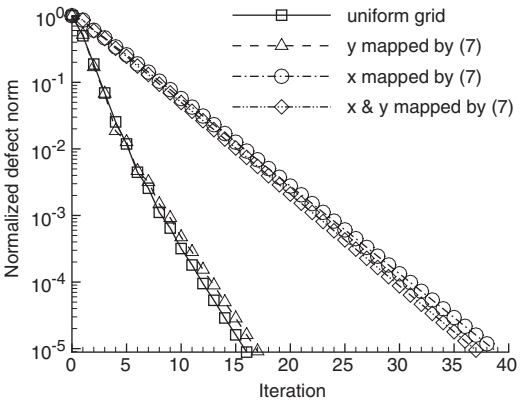

Figure 6. The effect of the grid mapping (7) on the convergence rate for Mode 1. The rest of the conditions are as in Figure 4.

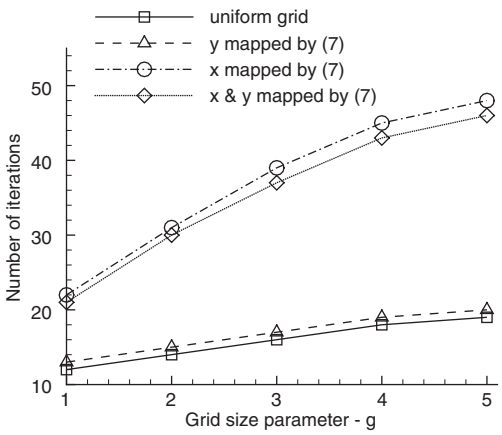

Figure 7. The effect of the grid size on the number of iterations it takes to get a normalized defect norm less than 10^{-5} and for Mode 1. The number of points of the grid is $(N_x, N_y) = (32, 16)2^{g-1} + (1, 1)$. The rest of the conditions are as in Figure 4.

on the convergence is shown in Figure 7. As in Figure 4 it shows the number of iterations needed to yield a normalized defect norm less than 10^{-5}. It is seen that the effect of the grid size is weak for the uniform grid and the grid with the stretched y direction. Thus as in the uniform grid without a rigid body the number of operations is still proportional to $N_x N_y \log_2(N_x)$, but with a coefficient in the order of 20 multiplying it for the particular case of Figure 7. On the other hand, the grids with a non-uniform x direction show higher dependence on the grid size, although that dependence decreases as the grid size increases.

Up till now all results were shown for the same aspect ratios of the computational domain $L_x/L_y = 2$ and the grid size $(N_x - 1)/(N_y - 1) = 2$. The effects of variations in these aspect ratios

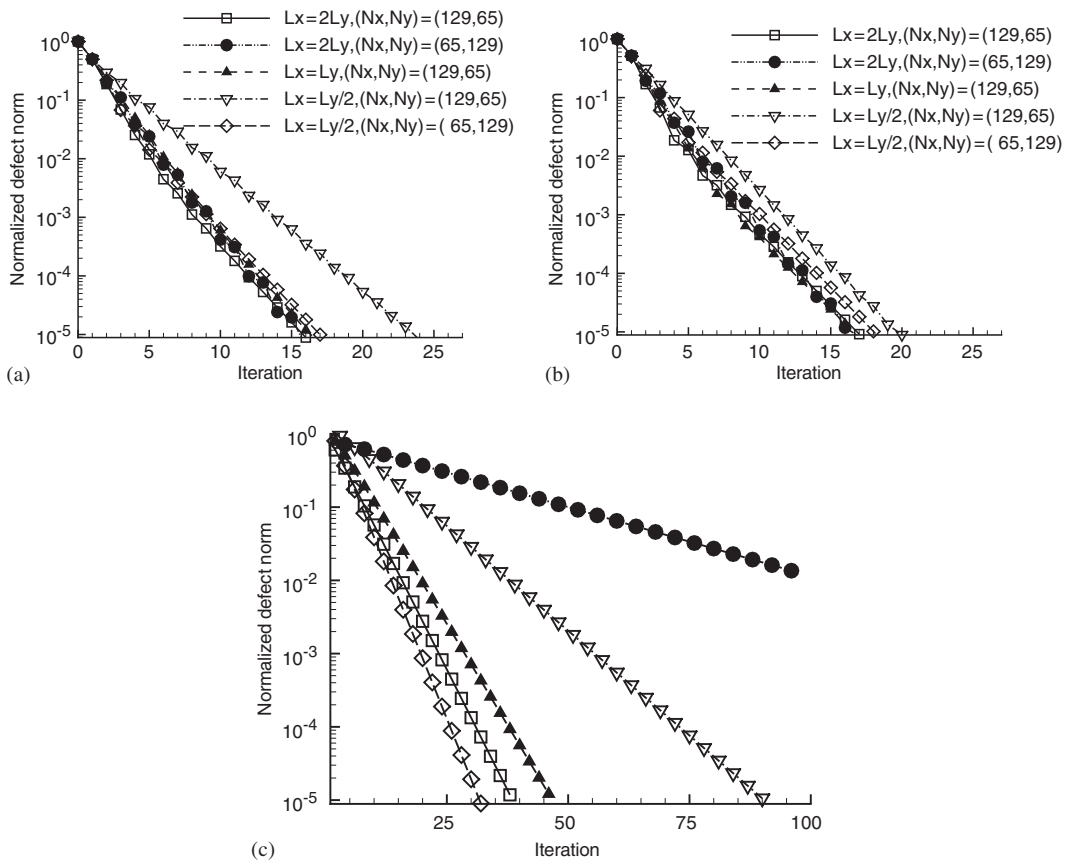

Figure 8. The effect of the aspects ratios of the computational domain and the grid size on the convergence rate for: (a) a uniform grid; (b) a stretched grid by (7) in the y direction; and (c) a stretched grid by (7) in the x direction. The Poisson source is of Mode 1 and the legend in (c) is the same in (a) and (b). The rest of the conditions are as in Figure 4.

are shown in Figure 8. The results for the uniform grids are in Figure 8(a) and they show only a very weak dependence on the aspect ratios as long as they are kept less than 1–4. Further numerical experimentation showed that increasing the aspect ratio of the computational domain to 1–8 did not show any significant change. However, the convergence rate deteriorates when $\Delta y/\Delta x = 4$ which is the case of $L_x = L_y/2$ and $(N_x, N_y) = (129, 65)$. This does not happen in the opposite case of $(N_x, N_y) = (65, 129)$. Further numerical experimentations for various aspect ratios of the computational domain confirmed the sensitivity to the high aspect ratio of $\Delta y/\Delta x$.

The sensitivity to the very coarse y direction can be reduced by using a grid mapping in this direction as demonstrated in Figure 8(b). By using a grid stretching factor of $\beta/\alpha = 1$, the convergence rate of $L_x = L_y/2$ and $(N_x, N_y) = (129, 65)$ becomes almost the same as the others. The case of a stretched x direction is shown in Figure 8(c). As found in earlier

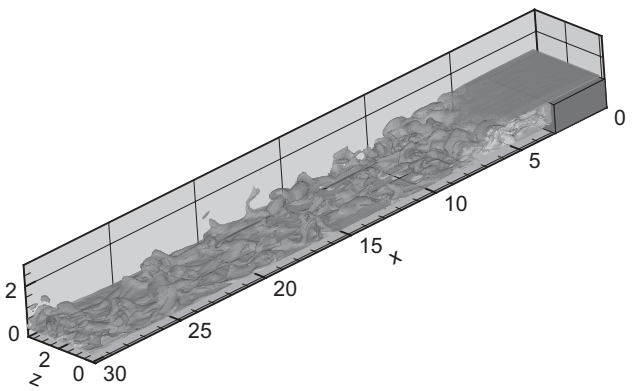

Figure 9. Instantaneous passive scalar iso-surfaces of levels 0.5 and 0.85 at time 160 for flow past a backward-facing step.

results it shows that a grid stretching in the FCT direction reduces in general the convergence rate. However, the most difficult case is now $L_x = 2L_y$ and $(N_x, N_y) = (65, 129)$. This case actually converged to the tolerance of 10^{-5} only after 250 iterations. This behaviour may be attributed to the high aspect ratios of some of the grid cells in the physical space that go up to $\Delta x/\Delta y = 8$. However, this level of aspect ratio or twice as much in the uniform grid did not yield such a strong deterioration in the convergence rate, indicating that the additional interaction between the modes due to the grid stretching in the FCT direction had a role in slowing the convergence. The case of $L_x = L_y/2$ and $(N_x, N_y) = (129, 65)$ also shows a relative low convergence rate, but all other three cases of the more moderate aspect ratios show similar and better convergence rates.

An example of flow simulation results that can be produced using the proposed FCT–tridiagonal solver is shown in Figure 9, where the step height h is normalized to 1. The time marching was achieved using a third-order compact Runge–Kutta, the convection terms were calculated using the Quick scheme and the diffusion terms were calculated using a central second-order scheme. Grid mapping was used in the y direction to cluster points at $y = 0$ and 1.5, with a stretching ratio of 2. The inflow condition was of a laminar boundary layer with a thickness $\delta = 0.2h$ and a random disturbance with 10% amplitude. The Reynolds number was set to $Re_h = 5000$ and the step was put at $0 \leqslant x \leqslant 3h$. The computational box size was set to $(30, 6, 3)h$ in the (x, y, z) directions, respectively, and a grid size of $(513, 120, 65)$ points. Free slip wall conditions were used at the top of the computational domain and at its spanwise sides. No slip wall conditions were used on the step boundaries and the bottom of the computational domain. Convective outflow conditions were used at the outlet $x = 30h$. The FCT algorithm was used in the x and z directions while the tridiagonal algorithm was used in the y direction. Additionally a passive scalar f_{ps} was simulated using its governing equation

$$\frac{\partial f_{\mathrm{ps}}}{\partial t} + \frac{\partial (f_{\mathrm{ps}} u_j)}{\partial x_j} = \frac{1}{ReSc} \frac{\partial^2 f_{\mathrm{ps}}}{\partial x_j \partial x_j} \tag{11}$$

where the Schmidt number Sc was taken as 1. The boundary conditions for the passive scalar were as of the streamwise velocity but without the inflow disturbance.

The simulation started from a zero flow initial condition and the inflow streamwise velocity was slowly increased until reaching its full value. The instantaneous iso-surfaces of the passive scalar are shown for time 160, where 1 time unit is defined as the time, the free stream takes to move a distance of $1h$. The flow clearly shows breakdown to small scales by going through a 3D breakdown of the large-scale wake mode near the step. This is a typical flow pattern in the backward-facing step configuration and the calculated mean reattachment length of $5.8h$ is in a good agreement with others, e.g. $6.28h$ from the DNS results of Le *et al.* [13] who used turbulent inflow conditions. Time history of the transverse velocity v at $x = 5h$ which is in the recirculation region, showed that the transition process was associated with a wave packet formation. The frequency of the amplitude modulation was of the wake mode $St_h \cong 0.06$ [13] and the higher frequency was about five times of that. Further analysis and comparisons to results from large eddy simulation (LES), detached eddy simulation (DES) and unsteady Reynolds averaged Navier–Stokes simulations (URANS) are presented in Reference [14].

3.2. The three-dimensional rigid body

Until now we looked at the two-dimensional body geometry where if a three-dimensional simulation is carried out, the third direction is dealt using the regular FCT algorithm. However bodies of three-dimensional geometry are of great interest and thus it is vital to see of there is a significant increase in the workload when using the proposed elliptic solver. Following the 2D body investigation the solver is initially assessed for an artificial Poisson source using

$$[u^*, v^*, w^*] = [\sin(k_x x)\cos(k_y y)\cos(k_z z),\ \cos(k_x x)\sin(k_y y)\cos(k_z z),\ \cos(k_x x)\cos(k_y y)\sin(k_z z)] \tag{12}$$

instead of the 2D velocity field specified in Equation (10). The FCT is applied in the x and z directions, where the tridiagonal solver is applied in the y direction. The wave numbers k_x, k_y and k_z are defined in the same way as in Equation (10).

The convergence rate was investigated for the case of a cube inside a cubic computational domain and is shown in Figure 10 for Mode 1, which as in the 2D case showed the lowest convergence rate. Comparing Figure 10 to its 2D counterpart Figure 6, shows that actually there is a decrease in the number of required iterations. This decrease is due to the specific location of the body and computational domain aspect ratio rather than a 3D effect as was verified when the cubic rigid body was turned into a square cylinder. As in the 2D case the grid mapping in the y direction which is the direction where the tridiagonal solver was used, did not change the convergence rate. The grid mapping in the FCT directions x and z, reduced the convergence rate by a factor of 2, which is similar to what happened in the 2D case.

The effect of the grid size is shown in Figure 11 for the 3D case. Again as in the 2D case the uniform grid and mapped grid in the y direction show much lower sensitivity to the grid size that the grids with a non-uniform FCT direction. However the slopes of the lines in Figure 11 are about half of their 2D counterparts in Figure 7, resulting for example,

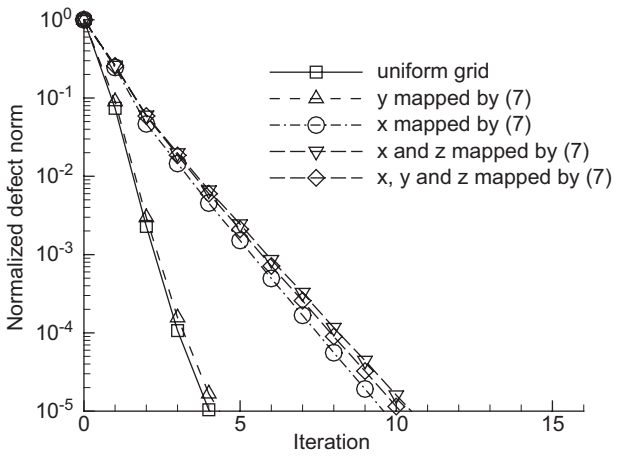

Figure 10. The convergence rate for Mode 1 of the three-dimensional Poisson source defined by Equation (12). The rigid body is a cube centred in a cubic computational domain of twice the length in each direction. The grid size is of $(33, 33, 33)$ points.

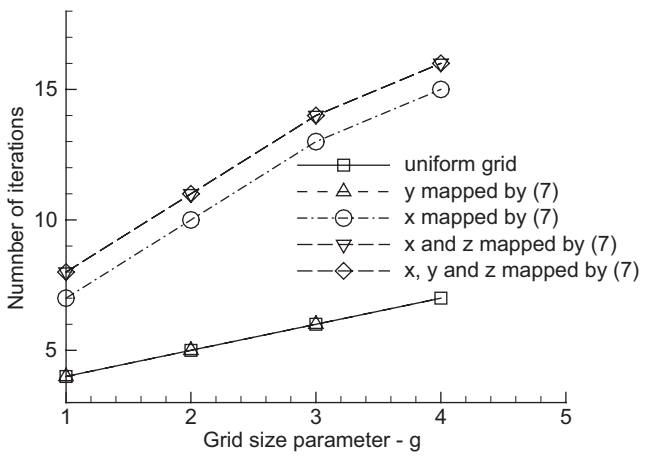

Figure 11. The effect of the grid size on the number of iterations required to get a normalized defect norm less than 10^{-5} for the 3D Mode 1. The number of grid points is $(16, 16, 16)2^{g-1} + (1, 1, 1)$ and the rest of the conditions are as in Figure 10.

in an increase of three iterations for the uniform grid when the grid size parameter g is increased from 1 to 4. The effect of the computational domain aspect ratio is demonstrated in Figure 12 for the uniform grid. It is seen that the best convergence is achieved for the cubic computational domain and the worst is when one of the domain lengths is smaller than the others. This is a behaviour already seen in the 2D case, see Figure 8(a) and the increase in the number of required iterations due to the change of the computational domain aspect ratio is similar. Thus one can conclude from Figures 10–12 that the behaviour of the

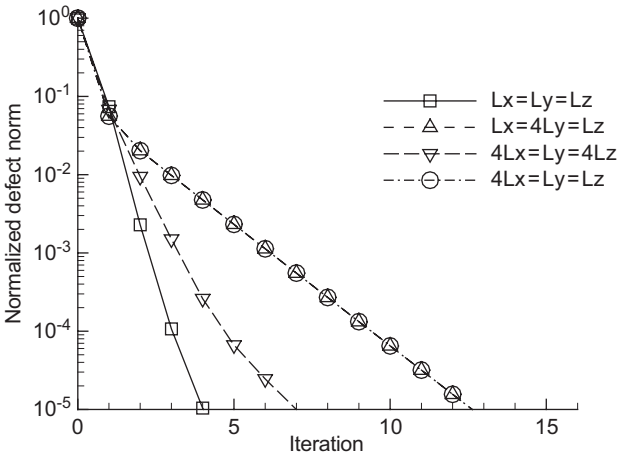

Figure 12. The effect of the computational domain aspect ratio on the rate of convergence for a uniform grid. The 3D rigid body is a box with a length half of that of the computational domain in each direction. The rest of the conditions are as in Figure 10.

solver in the 3D case is generally similar to that in the 2D case and a similar convergence rate is achieved. Of course the 3D case will require more time to compute since for each iteration the solver will have to perform $O(N_x N_y N_z \log_2(N_x) \log_2(N_z))$ operations as compared to $O(N_x N_y \log_2(N_x))$ operations in the 2D case.

To illustrate the 3D capability of the new solver, the NS equations were simulated using the LES approach for the case of a boundary layer encountering a rectangular 3D obstacle. The inflow boundary layer profile was set to $(y/\delta)^{1/7}$ where the free stream velocity was normalized to 1. The computational domain size was set to $(10, 4, 4)\delta$ and the grid size to $(129, 65, 65)$ points in the x, y and z directions, respectively. The rigid body was set at $3\delta \leqslant x \leqslant 5\delta$, $0 \leqslant y \leqslant \delta$ and $1.5\delta \leqslant z \leqslant 2.5\delta$ and a grid mapping was used to cluster points at $y = 0$ and δ similarly to the backward-facing step simulation. The sub-grid stress (SGS) model was Smagorinsky with $C_s = 0.17$ and it was coupled with an algebraic damping wall function [15]. The Reynolds number was set to $Re_\delta = 5000$ and the rest of the conditions and the method were as of the backward-facing step simulation.

The instantaneous iso-surface of the passive scalar is shown in Figure 13 for time 20, where 1 time unit is defined as δ/U_∞ and δ was normalized to 1 in the figure. A bow wave is observed in front of the obstacle and which goes around it to form two counteracting vortices from the two sides of the box. This is a typical behaviour of the flow past a 3D bluff body [16], however the current vortices are a bit further apart than in the PIV measurements of a 3D car model in Reference [16]. The flow already detaches from the top of the box before its end as can be seen from Figure 13 and as was also verified from longitudinal and lateral cross-sections of the flow field. This is unlike the detachment of the flow in the backward-facing step that occurred only after the end of the body and it is associated with the longitudinal vortices developing on the sides of the box. In general the wake shows more longitudinal structures than the wake of the backward-facing step and this is a characteristic of a wake of a 3D bluff body [16].

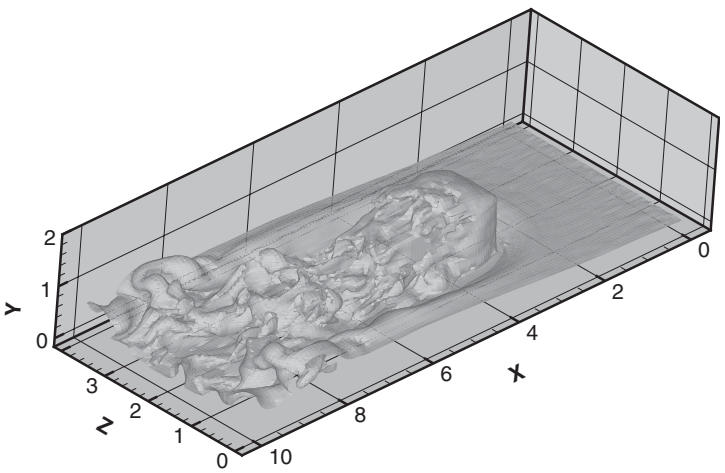

Figure 13. Instantaneous passive scalar iso-surface of level 0.75 and at time 20 for a boundary layer flow past a box located at $3 \leqslant x \leqslant 5$, $0 \leqslant y \leqslant 1$ and $1.5 \leqslant z \leqslant 2.5$, where the incoming boundary layer thickness was normalized to 1.

The method was further tested for open 3D cavity and 2D wall barrier geometry, all showed a similar behaviour to the one found for the step and box configurations. A limited comparison to the BCG method was also carried out. The performance of the latter depends considerably on the solver of the preconditioned form. When the easy-to-program diagonal scaling solver was used, the present method showed a much superior performance except for the extreme aspect ratio in Figure 8(c), where the performance of both methods was similar. The new elliptic solver also generally showed better performance when a simple ILU pre-conditioner solver was used. When the pre-conditioner solver was replaced by one iteration of the proposed FCT–tridiagonal solver, the performance of the two solvers was similar for the uniform grid, with a slight advantage for the current method. However, in the case of a non-uniform grid in any direction the convergence of the BCG method was unsatisfactory. It points to the need to modify the current FCT–tridiagonal solver to the transpose matrix equation if it is to be used for the BCG method, as it was discussed in Section 2.2. A comparison to the geometric multigrid method was not pursued due to the problem of the coarser grids to capture the right location of the rigid body.

4. SUMMARY

The numerical solution of the Poisson equation on a rectangular staggered grid was pursued by using a combination of the fast cosine transform (FCT) method and a tridiagonal solver. A solution of the Poisson equation is required, for example, when the incompressible N–S equations are simulated using the projection method. The technique of combining FCT with a tridiagonal solver was extended for cases where the boundaries of the flow regime do not coincide with the boundaries of the computational domain and for grids that are non-uniform in more than one direction. The new technique is an iterative procedure that is based on

solving the defect equation using the FCT–tridiagonal solver and which is followed by a few iterations of the relaxation procedure of the point Gauss–Zeidel method. Analysis of the one-dimensional case showed that the solution converged as a geometric series provided that interactions between the modes did not interfere. The one-dimensional case was further investigated to find that the grid stretching factor in the direction of the FCT should be limited to the order of 1 for practical use.

Test cases for rigid bodies of a 2D step and a box configurations, confirmed the geometric series convergence. It was also found that the long waves took the longest to converge. The new method was found to be effective particularly for the uniform grid and the grid with a non-uniform direction where the tridiagonal solver was used. The convergence rate was similar in both cases and it showed only a weak dependency on the grid size. The grids that were non-uniform in the direction where the FCT was used showed a lower convergence rate and a higher dependency on the grid size.

The method showed a very weak dependency on the grid cell aspect ratio as long as it was less than 4. Aspect ratios higher than this level were found capable to cause deterioration in the convergence rate in the 2D step configuration when the direction of the tridiagonal solver was coarser than the direction of the FCT. Grid mapping in the direction of the tridiagonal solver was found to be capable of restoring the convergence rate, since it resulted in a variable grid cell aspect ratio. It should be noted that deterioration in the performance due to a high aspect ratio in the grid cell also happens in other methods as the BCG and multigrid. Furthermore, practically the direction of the tridiagonal solver will be usually finer than the other directions as for example in the case of a boundary layer simulation. In that case no strong deterioration in the convergence rate can be expected even for grid cell aspect ratio high as 8 as mentioned in Section 3.1.

The new solver was further illustrated by incorporating it with the DNS and LES techniques to simulate flow separation and vortex shedding occurring in the cases of a backward-facing step and a 3D rectangular obstacle. It was demonstrated that the elliptic solver was not limited to a specific grid mapping in the tridiagonal solver direction and the results compared qualitatively well with published results. A limited comparison to the BCG method showed a superior performance by the proposed method.

This newly proposed method can be further investigated by further comparisons to other elliptic solvers, nevertheless its effectiveness has already been demonstrated. It is capable of dealing with wall conditions whether free or no slip and periodic boundary conditions just require replacing the FCT algorithm with the FFT algorithm while keeping the rest intact. It can also be used for free flows, e.g. the free jet simulations of Alonso and Avital [17], whose high resolution results are to be reported. Further use of the new technique is planned for exploring the effects of turbulence fluctuations on sound propagation in the presence of rigid bodies by coupling the incompressible N–S solver with an acoustic equations solver [18].

APPENDIX A: THE EFFECT OF THE RIGID BODY IN THE ONE-DIMENSIONAL CASE

Consider the following 1D Poisson equation

$$\frac{\mathrm{d}^2 p}{\mathrm{d}x^2} = F, \quad 0 \leqslant x \leqslant L \tag{A1}$$

where

$$F = \begin{cases} \cos(\gamma_m x), & 0 \leqslant x \leqslant c \\ 0, & c < x \leqslant L \end{cases} \tag{A2}$$

and $\gamma_m \equiv m\pi/c$. The boundary conditions are $\mathrm{d}p/\mathrm{d}x = 0$ at $x = 0, c$. The segment $c < x < L$ represents the rigid body and thus it can also be assumed that $\mathrm{d}p/\mathrm{d}x = 0$ at $x = L$. Since a uniform grid is used, L/c must be a rational number. Therefore γ_m must be equal to a certain wave number k_n that is defined as $n\pi/L$. Applying the suggested iterative method of Section 2.2 means that the cosine transform has to be applied to all the section $0 < x < L$. Thus after one iteration one gets

$$\hat{p}_n^1 = -\frac{c}{k_n^2 L} \tag{A3}$$

where the cosine transform was performed analytically in the continuous limit. The hat denotes a cosine transform, the superscript 1 means after the first iteration and the subscript denotes the mode number. If the relaxation stage is not performed then the residual in the mode n will be $\hat{d}_n^1 = 1 - c/L$, leading to

$$\hat{p}_{n\to n}^2 = -\frac{c}{k_n^2 L}\left(1 - \frac{c}{L}\right) \tag{A4}$$

The subscript $n \to n$ means that only the effect of the mode n in the residual was considered in the pressure solution of the mode n. Continuing with this process and summing all the pressure solutions of the defect equations, leads to

$$\hat{p}_n = -\frac{c}{k_n^2 L}\left[1 + \left(1 - \frac{c}{L}\right) + \left(1 - \frac{c}{L}\right)^2 + \cdots\right] \tag{A5}$$

This is a geometric series and since $c/L < 1$, it converges to $-1/k_n^2$, which is the analytical answer.

In this analysis the interactions between the mode n and other modes due to the discontinuity at $x = c$ were neglected. This discontinuity causes Gibb's phenomenon and the interaction happens in modes where the ratio c/L times the mode number does not yield an integer. The analytical investigation of this effect is left for future work due to the complexity of the interactions between the modes. Nevertheless, as remarked in Section 2 the relaxation procedure of Gauss–Zeidel was found to be an effective tool in suppressing those interactions.

ACKNOWLEDGEMENTS

The author wishes to thank EPSRC for their support to CFD research through grants GR/R64947/01 and GR/SR46239/01.

REFERENCES

1. Peyret P, Taylor TD. *Computational Methods for Fluid Flow*. Springer: New York, 1983; 143–166.
2. Avital EJ, Sandham ND, Luo KH. Stretched Cartesian grids for solution of the incompressible Navier–Stokes equations. *International Journal for Numerical Methods in Fluids* 2000; **33**:897–918.

3. Meitz HL, Fasel HF. A compact difference scheme for the Navier–Stokes equations in vorticity–velocity formulation. *Journal of Computational Physics* 2000; **157**:371–400.
4. Kim WW, Menon S. An unsteady incompressible Navier–Stokes solver for large eddy simulation. *International Journal for Numerical Methods in Fluids* 1999; **31**:983–1017.
5. Kim J, Moin P. Application of a fractional-step method to incompressible Navier–Stokes equations. *Journal of Computational Physics* 1985; **58**:308–322.
6. Press WH, Teukolsky SA, Vettering WT, Flannery BP. *Numerical Recipes in Fortran* 1992; 848–854.
7. Cain AB, Ferziger JH, Reynolds WC. Discrete orthogonal function expansions for non-uniform grids using the fast Fourier transform. *Journal of Computational Physics* 1984; **56**:272–286.
8. Buell JC. A hybrid numerical method for three dimensional spatially-developing free-shear layers. *Journal of Computational Physics* 1995; **95**:313–338.
9. Thomas TG, Williams JJR. Simulation of turbulent flow past a surface mounted cube. *Journal of Wind Engineering* 1999; **81**:347–360.
10. Avital EJ, Musafir RE. Simulations of flow and sound fields for acoustic barrier in the presence of wind. In *10th International Congress on Sound and Vibration*, *Proceedings of ICSV10* 2003; 1461–1468.
11. Avital EJ, Musafir RE. Flow patterns and sound generation in low speed cavities. In *Direct and Large Eddy Simulation V*, Friedrich R, Metais O, Geurts BJ (eds). Kluwer Academic Publishers: Dordrecht, 2003; 431–438.
12. Le H, Moin P. An improvement of fractional step methods for the incompressible Navier–Stokes equations. *Journal of Computational Physics* 1991; **92**:369–379.
13. Le H, Moin P, Kim J. Direct numerical simulation of turbulent flow over a backward facing step. *Journal of Fluid Mechanics* 1997; **330**:349–374.
14. Mercier E, Avital EJ. Detached eddy simulation and flow over a backward-facing step. *Computers and Fluids*, submitted.
15. Mason P, Thomson DJ. Stochastic backscatter in large eddy simulations of boundary layers. *Journal of Fluid Mechanics* 1992; **242**:51–78.
16. Bearman PW. Near wake flows behind two- and three-dimensional bluff bodies. *Journal of Wind Engineering* 1997; **69–71**:33–54.
17. Alonso M, Avital EJ. Basic sound radiation from large scale structures in circular and elliptical jets. *AIAA Paper 2004-3027*, 2004.
18. Avital EJ. Computation of sound in free and wall bounded domains. *Journal of Sound Vibration* 2004; **270**(3):483–494.

